Shock-like structures in the tropical cyclone boundary layer

Gabriel J. Williams,[1] Richard K. Taft,[2] Brian D. McNoldy,[3] and Wayne H. Schubert[2]

Received 13 November 2012; revised 26 March 2013; accepted 1 April 2013.

[1] This paper presents high horizontal resolution solutions of an axisymmetric, constant depth, slab boundary layer model designed to simulate the radial inflow and boundary layer pumping of a hurricane. Shock-like structures of increasing intensity appear for category 1–5 hurricanes. For example, in the category 3 case, the $u(\partial u/\partial r)$ term in the radial equation of motion produces a shock-like structure in the radial wind, i.e., near the radius of maximum tangential wind the boundary layer radial inflow decreases from approximately 22 m s^{-1} to zero over a radial distance of a few kilometers. Associated with this large convergence is a spike in the radial distribution of boundary layer pumping, with updrafts larger than 22 m s^{-1} at a height of 1000 m. Based on these model results, it is argued that observed hurricane updrafts of this magnitude so close to the ocean surface are attributable to the dry dynamics of the frictional boundary layer rather than moist convective dynamics. The shock-like structure in the boundary layer radial wind also has important consequences for the evolution of the tangential wind and the vertical component of vorticity. On the inner side of the shock the tangential wind tendency is essentially zero, while on the outer side of the shock the tangential wind tendency is large due to the large radial inflow there. The result is the development of a U-shaped tangential wind profile and the development of a thin region of large vorticity. In many respects, the model solutions resemble the remarkable structures observed in the boundary layer of Hurricane Hugo (1989).

Citation: Williams, G. J., R. K. Taft, B. D. McNoldy, and W. H. Schubert (2013), Shock-like structures in the tropical cyclone boundary layer, *J. Adv. Model. Earth Syst.*, *5*, doi:10.1002/jame.20028.

1. Introduction

[2] The red curves in Figure 1 show aircraft data from a low level (434 m average height), southwest to northeast radial penetration of Hurricane Hugo on 15 September 1989 (see *Marks et al.* [2008] and *Zhang et al.* [2011] for detailed discussions). As the aircraft flew inward through the lower portion of the eyewall, the tangential wind increased from 50 m s^{-1} near $r = 22$ km to a maximum of 88 m s^{-1} just inside $r = 10$ km. Near the inner edge of the eyewall there were multiple updraft-downdraft couplets (the strongest updraft just exceeding 20 m s^{-1}), with associated oscillations of the radial and tangential velocity components and a very rapid 60 m s^{-1} change in tangential velocity near 7 km radius. After ascending in the eye, the aircraft departed the eye to the northeast (2682 m average height), obtaining the horizontal and vertical velocity data shown by the blue curves in Figure 1. The extreme horizontal wind shears and large vertical velocities observed at 434 m in the southwest sector were not observed at 2682 m in the northeast sector. Since these extreme structures in the boundary layer wind field occur under a region of high radar reflectivity, it is natural to attribute them to moist convective dynamics. For example, the large updrafts could be attributed to nonhydrostatic vertical accelerations associated with latent heat release, and the large potential vorticity at $r = 7$ km could be attributed to the diabatic source term in the potential vorticity equation. However, the purpose of the present paper is to explore the possibility that the type of behavior seen in Figure 1 can be explained by nonlinear effects that occur in a simple dry model of the hurricane boundary layer. In the following analysis we shall interpret the blue tangential wind curve in Figure 1 as an inviscid, axisymmetric gradient balanced flow whose associated radial pressure gradient is also felt in the frictional boundary layer below. We then interpret the red tangential wind curve as an axisymmetric frictional boundary layer flow (driven by the same radial pressure gradient) that is supergradient inside $r \approx 13$ km and subgradient outside this radius. The subgradient/supergradient nature of the boundary layer flow is closely related to the magnitude of the $u(\partial u/\partial r)$ term in the radial equation of motion.

[1]Department of Atmospheric Sciences, University of Louisiana at Monroe, Monroe, Louisiana, USA.
[2]Department of Atmospheric Science, Colorado State University, Fort Collins, Colorado, USA.
[3]Rosenstiel School of Marine and Atmospheric Science, University of Miami, Miami, Florida, USA.

1942-2466/13/10.1002/jame.20028

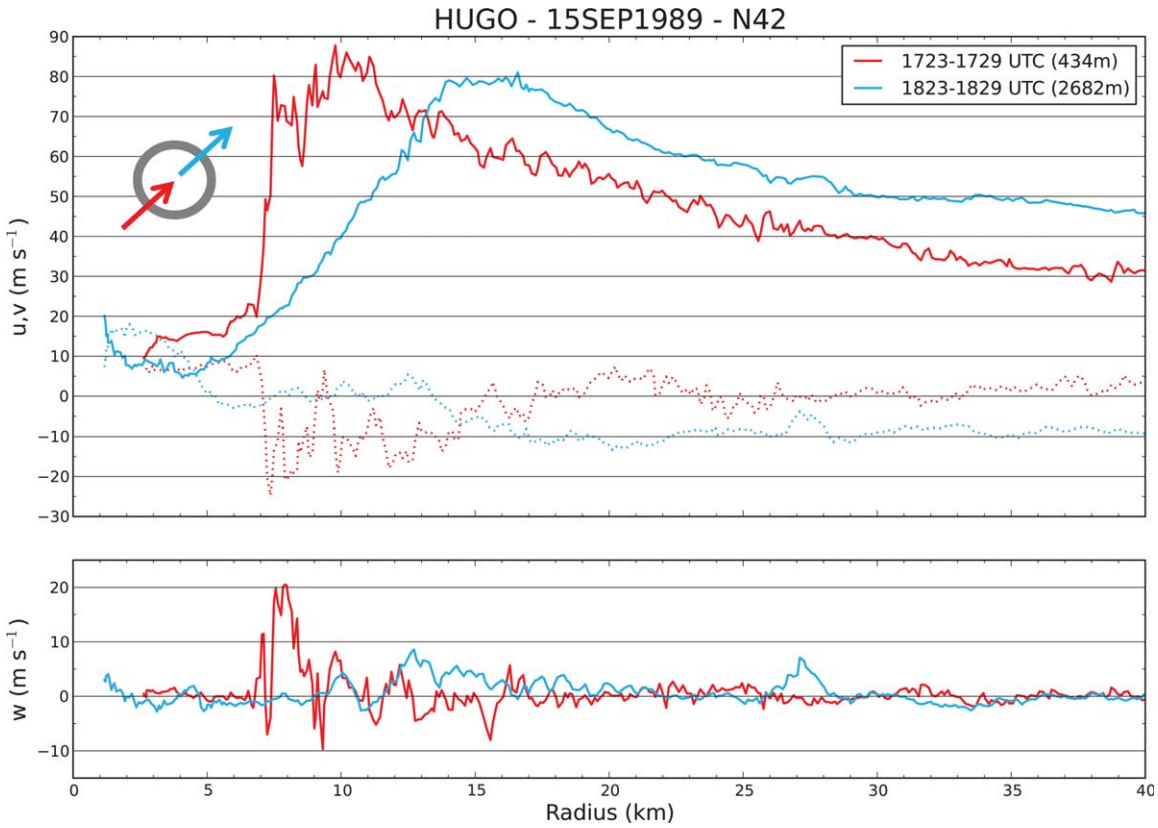

Figure 1. NOAA WP-3D (N42RF) aircraft data from an inbound leg in the southwest quadrant (red, 434 m average height) and an outbound leg in the northeast quadrant (blue, 2682 m average height) of Hurricane Hugo on 15 September 1989. (top) The solid curves show the tangential wind component, while the dotted curves show the radial wind component. (bottom) The vertical component of the velocity. These radial profiles are based on 1 s flight data, which corresponds to a spatial resolution of approximately 100 m. Due to severe boundary layer turbulence in the eyewall region, there were excursions from the 434 m average height of the inbound leg, with heights of 456, 359, 274, 269, 361, 433, 422, and 396 m for radii of 4.0, 5.0, 6.0, 6.2, 7.0, 8.0, 9.0, and 10.0 km, respectively. This flight data was obtained from the NOAA Hurricane Research Division of the Atlantic Oceanographic and Meteorological Laboratory.

We shall also argue that this term is responsible for the shock-like structure that occurs near $r = 7$ km.

[3] As a theoretical basis for the above arguments we shall use the axisymmetric, primitive equation version of the slab boundary layer model used in many studies of the hurricane boundary layer. For further discussion of the model and its application to many aspects of tropical cyclone dynamics, the reader is referred to *Ooyama* [1969a, 1969b], *Anthes* [1971], *Chow* [1971], *Yamasaki* [1977], *Shapiro* [1983], *Emanuel* [1997], *Smith* [2003], *Smith and Vogl* [2008], *Smith and Montgomery* [2008, 2010], *Smith et al.* [2008], *Smith and Thomsen* [2010], and *Kepert* [2010a, 2010b]. The emphasis here is on interpreting the observations shown in Figure 1 in terms of "Burgers' shock-like" structures that emerge from the fact that the radial boundary layer equation contains an embedded Burgers' equation. An excellent general mathematical discussion of Burgers' shock effects can be found in the book by *Whitham* [1974], which includes a review of the original work by *Burgers* [1948], *Hopf* [1950], and *Cole* [1951].

[4] This paper is organized in the following way. Section 2 presents the governing set of partial differential equations (PDEs) for the slab model. Section 3 discusses the shock-like structures that appear in the model solutions. Section 4 gives some reinterpretations of other low-level aircraft data and of previously published nonhydrostatic, moist model simulations. Section 5 contains some concluding remarks on shock-like structures in more general settings such as translating vortices.

2. Primitive Equation Slab Boundary Layer Model

[5] We consider axisymmetric motions of an incompressible fluid on an f-plane. The frictional boundary layer is assumed to have constant depth h, with radial and azimuthal velocities $u(r, t)$ and $v(r, t)$ that are independent of height between the top of a thin surface layer and height h, and with vertical velocity $w(r, t)$ at height h. The horizontal velocity components are

discontinuous across the top of the boundary layer. In the overlying layer, the radial velocity is assumed to be negligible and the azimuthal velocity $v_{gr}(r)$ is assumed to be in gradient balance and to be constant in time. The boundary layer flow is driven by the same radial pressure gradient force that occurs in the overlying fluid, so that in the radial equation of boundary layer motion, the pressure gradient force can be expressed as the specified function $\left(f+v_{gr}/r\right)v_{gr}$. The governing system of differential equations for the boundary layer variables $u(r,t)$, $v(r,t)$, and $w(r,t)$ then takes the form

$$\frac{\partial u}{\partial t}=-u\frac{\partial u}{\partial r}-w^{-}\left(\frac{u}{h}\right)+\left(f+\frac{v+v_{gr}}{r}\right)(v-v_{gr})-c_D U\frac{u}{h} +K\frac{\partial}{\partial r}\left(\frac{\partial(ru)}{r\partial r}\right), \tag{1}$$

$$\frac{\partial v}{\partial t}=w^{-}\left(\frac{v_{gr}-v}{h}\right)-\left(f+\frac{\partial(rv)}{r\partial r}\right)u-c_D U\frac{v}{h} +K\frac{\partial}{\partial r}\left(\frac{\partial(rv)}{r\partial r}\right), \tag{2}$$

$$w=-h\frac{\partial(ru)}{r\partial r}, \tag{3}$$

where

$$U=0.78\left(u^2+v^2\right)^{1/2} \tag{4}$$

is the wind speed at 10 m height, which is assumed to be 78% of the mean boundary layer wind speed (as supported by the dropwindsonde data of *Powell et al.* [2003]), and $w^{-}=\frac{1}{2}(|w|-w)$ is the rectified Ekman suction. Concerning the dependence of the drag coefficient c_D on wind speed, we use

$$c_D=10^{-3}\begin{cases}2.70/U+0.142+0.0764U & \text{if } U\le 25\\ 2.16+0.5406\{1-\exp[-(U-25)/7.5]\} & \text{if } U\ge 25,\end{cases} \tag{5}$$

where the 10 m wind speed U is expressed in m s^{-1}. The $U\le 25$ m s^{-1} part of equation (5) is based on *Large et al.* [1994] and has been constructed to make c_D go to its theoretical infinite value at zero wind speed. The $U\ge 25$ m s^{-1} part of equation (5) is based on *Powell et al.* [2003] and *Donelan et al.* [2004], who argue that c_D reaches a saturation value between 2.5×10^{-3} and 2.8×10^{-3} for high wind speeds. A physical explanation of this saturation effect can be found in *Reul et al.* [1999], who experimentally studied the phenomenon of air flow separation over unsteady breaking waves. The numerical values of the constants in the $U\ge 25$ m s^{-1} part of equation (5) guarantee that c_D and its first derivative are continuous at $U=25$ m s^{-1}. A plot of c_D versus U from equation (5) is shown by the red curve in Figure 2, while a plot of $c_D U$ versus U is shown by the red curve in Figure 3. It should be noted that the high wind speed behavior of the surface exchange coefficients for momentum and enthalpy remains one of the most uncertain aspects of tropical cyclone models. For further discussion of this uncertainty and its implications for intensity prediction, see *Emanuel* [2003], *Moon et al.* [2004], *Bender et al.* [2007], *Haus et al.* [2010], and *Andreas et al.* [2012].

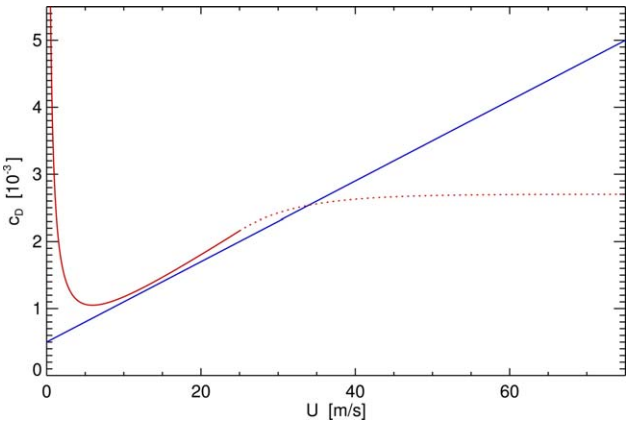

Figure 2. The drag coefficient c_D as a function of the wind speed at a height of 10 m. The solid red curve is from the top line of equation (5) and is based on *Large et al.* [1994]. The dotted red curve is from the bottom line of equation (5) and is based on the work of *Powell et al.* [2003] and *Donelan et al.* [2004]. For comparison the blue curve is $c_D=10^{-3}(0.5+0.06U)$, which was used in the tropical cyclone model of *Ooyama* [1969a].

[6] Since equations (1) and (2) may have a somewhat unfamiliar form, a derivation from first principles is given in Appendix A. Concerning the boundary conditions for equations (1) and (2), we require that

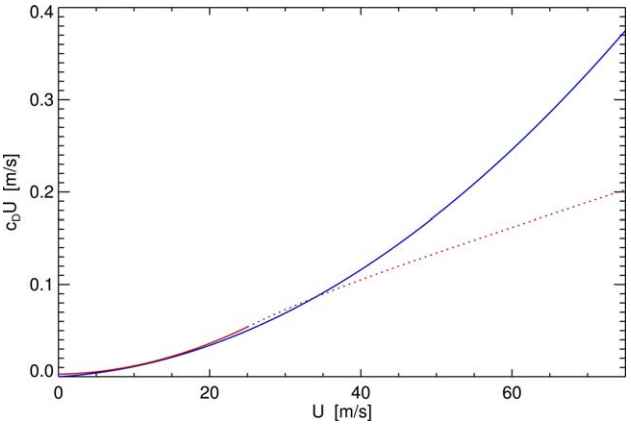

Figure 3. The red curve displays the drag factor $c_D U$ as a function of U based on formula (5), while the blue curve shows a similar plot based on the formula $c_D=10^{-3}(0.5+0.06U)$ as was used in the tropical cyclone model of *Ooyama* [1969a].

$$\left.\begin{array}{l} u=0 \\ v=0 \end{array}\right\} \text{ at } r=0,$$
$$\left.\begin{array}{l} \dfrac{\partial(ru)}{\partial r}=0 \\ \dfrac{\partial(rv)}{\partial r}=0 \end{array}\right\} \text{ at } r=b, \tag{6}$$

where b is the radius of the outer boundary. The initial conditions $u(r,0)$ and $v(r,0)$ and the forcing $v_{gr}(r)$ are discussed in section 3.

[7] It is interesting to note that the first numerical model capable of simulating a hurricane life cycle [*Ooyama*, 1969a] used highly simplified boundary layer dynamics. The three-layer model employed the gradient balance approximation in all three layers, so that the boundary layer radial wind equation (1) was replaced by $v=v_{gr}$ and the boundary layer tangential wind equation (2) was replaced by

$$hu=-\frac{c_D|v_{gr}|v_{gr}}{f+\zeta_{gr}}, \tag{7}$$

where $\zeta_{gr}=\partial\left(rv_{gr}\right)/r\partial r$ is the relative vorticity of the gradient wind. Equation (7) is a local balance that, when used in equation (3), gives the simple boundary layer pumping formula:

$$w=\frac{\partial}{r\partial r}\left(\frac{c_D|v_{gr}|rv_{gr}}{f+\zeta_{gr}}\right). \tag{8}$$

Because of the neglect of the $u(\partial u/\partial r)$ term, this model obviously does not capture Burgers' shock effects. Although his model yielded fairly reasonable numerical simulations of hurricane life cycles, Ooyama realized that the use of gradient balance in the calculation of the boundary layer inflow was probably the weakest assumption in the model. When the boundary layer radial inflow is strong, the neglect of the radial advection term $u(\partial u/\partial r)$ in equation (1) is not justifiable (see *Smith et al.* [2008] for an extensive discussion).

[8] In a companion study, *Ooyama* [1969b] relaxed the assumption of gradient balance in the boundary layer in order to produce a more accurate radial distribution of boundary layer pumping. In the improved model, the boundary layer radial wind equation (1) was replaced by

$$u\frac{\partial u}{\partial r}=\left(f+\frac{v+v_{gr}}{r}\right)\left(v-v_{gr}\right)-\frac{(c_DU+w^-)u}{h}, \tag{9}$$

and the boundary layer tangential wind equation (2) was replaced by

$$u\left(f+\frac{\partial(rv)}{r\partial r}\right)=-\frac{c_DUv+w^-\left(v-v_{gr}\right)}{h}, \tag{10}$$

so now the determination of u, v, and the corresponding boundary layer pumping w involves the solution of coupled equations, one of which is a first-order differential equation involving $u(\partial u/\partial r)$ and the other of which is a first-order differential equation involving $u[f+\partial(rv)/r\partial r]$. Ooyama solved this coupled problem by inward numerical integration using appropriate boundary conditions on u and v at large radius (1000 km). No boundary conditions were imposed at $r=0$, but u and v were found to approach zero as $r\to 0$. This improved model has the ingredients necessary to produce a shock but, because of the lack of horizontal diffusion, may produce multivalued solutions in some cases, depending on the numerical methods used.

[9] When this improved boundary layer model was incorporated into the complete three-layer hurricane model, some interesting changes in the hurricane life cycle were obtained. With the inclusion of the $u(\partial u/\partial r)$ term in the boundary layer radial momentum equation, the peak boundary layer pumping lies on the inside edge of the eyewall rather than on the outside edge of the eyewall. This places the diabatic heating closer to the region of high inertial stability so that the storm's maximum wind increases more rapidly and the central pressure falls more rapidly. These results are consistent with the notion that intensification depends crucially on the spatial proximity of the maximum values of inertial stability and diabatic heating (further discussion is given by *Musgrave et al.* [2012, and references therein]).

[10] Although *Ooyama* [1969b] did not report any problems with the inward numerical integration procedure, *Smith* [2003] and *Smith and Vogl* [2008] have discovered a striking failure of the procedure, which occurs when the radial wind begins to wildly oscillate near the radius of maximum gradient wind. Similar difficulties have been described by *Kepert* [2010a, 2010b]. Such difficulties are associated with the tendency of these equations to produce a Burgers' shock in the u field. In the absence of horizontal diffusion or some type of shock fitting procedure, the inward radial integration procedure generally fails. For this reason, we have included in the boundary layer equations (1) and (2) both time dependence and horizontal diffusion, so that the problem can be treated as a well-posed initial value problem describing the time-dependent approach to a steady-state solution with a Burgers' shock.

[11] Before proceeding to the discussion of model results, it is worthwhile to note that the boundary layer model domain does not constitute an energetically closed domain. The kinetic energy principle associated with the slab boundary layer model (1)–(6) is obtained by multiplying equation (1) by u and equation (2) by v and then adding the resulting equations to obtain

$$\begin{aligned} &\frac{\partial\left[\frac{1}{2}h\left(u^2+v^2\right)\right]}{\partial t}+\frac{\partial\left[\frac{1}{2}hru\left(u^2+v^2\right)\right]}{r\partial r}+\frac{1}{2}w^+\left(u^2+v^2\right) \\ &\quad -w^-\left[vv_{gr}-\tfrac{1}{2}\left(u^2+v^2\right)\right]+hu\left(f+\frac{v_{gr}}{r}\right)v_{gr} \\ &=-c_DU\left(u^2+v^2\right)+hK\left(\frac{\partial[r(u\delta+v\zeta)]}{r\partial r}-\delta^2-\zeta^2\right), \end{aligned} \tag{11}$$

where $\delta=\partial(ru)/r\partial r$ is the divergence and $\zeta=\partial(rv)/r\partial r$ is the relative vorticity. Integrating equation (11) over the entire area and using the boundary conditions (6), we obtain

$$\frac{d\mathcal{K}}{dt}=\mathcal{F}+\mathcal{G}-\mathcal{D}, \tag{12}$$

where the kinetic energy $\mathcal{K}$, the flux $\mathcal{F}$, the generation $\mathcal{G}$, and the dissipation $\mathcal{D}$ are given by

$$\mathcal{K}=h\int_0^b \frac{1}{2}\left(u^2+v^2\right)r\,dr,$$

$$\mathcal{F}=\int_0^b \left\{w^-\left[vv_{gr}-\frac{1}{2}\left(u^2+v^2\right)\right]-\frac{1}{2}w^+\left(u^2+v^2\right)\right\}r\,dr - \left[\frac{1}{2}hru\left(u^2+v^2\right)\right]_{r=b},$$

$$\mathcal{G}=-h\int_0^b u\left(f+\frac{v_{gr}}{r}\right)v_{gr}\,r\,dr=-h\int_0^b \frac{u}{\rho}\frac{\partial p}{\partial r}\,r\,dr,$$

$$\mathcal{D}=\int_0^b \left[c_D U\left(u^2+v^2\right)+hK\left(\delta^2+\zeta^2\right)\right]r\,dr. \tag{13}$$

[12] To summarize, the total kinetic energy of the boundary layer changes in time due to vertical and lateral fluxes at the top and outer boundaries ($\mathcal{F}$), the generation of kinetic energy by inward radial flow down the pressure gradient ($\mathcal{G}$), and the dissipation due to surface drag and lateral diffusion ($\mathcal{D}$). Numerical experience shows that the quasi-steady-state hurricane boundary layer is characterized by an approximate balance between the $\mathcal{G}$ term and the surface drag part of the $\mathcal{D}$ term. Thus, although the lateral diffusion terms in equations (1) and (2) will turn out to be important near the Burgers' shock, they play a minor role in the overall boundary layer energetics.

3. Model Results

[13] The problem (1)–(6) has been solved using centered, second-order, spatial finite difference methods on the domain $0 \le r \le 1000$ km with a uniform radial grid spacing of 100 m and a fourth-order Runge-Kutta time differencing scheme with a time step of 1 s. To illustrate how the radial flow $u(r,t)$, the tangential flow $v(r,t)$, and the boundary layer pumping $w(r,t)$ evolve into a steady state, the initial conditions have been chosen to be $u(r,0)=0$ and $v(r,0)=v_{gr}(r)$, and the constants have been chosen as $h=1$ km, $f=5.0\times10^{-5}$ s^{-1}, and $K=1500$ m^2 s^{-1}. The choice of K is discussed further in Appendix B. The forcing $v_{gr}(r)$ is specified through its associated vorticity $\zeta_{gr}(r)=d\left[rv_{gr}(r)\right]/rdr$, which has the form

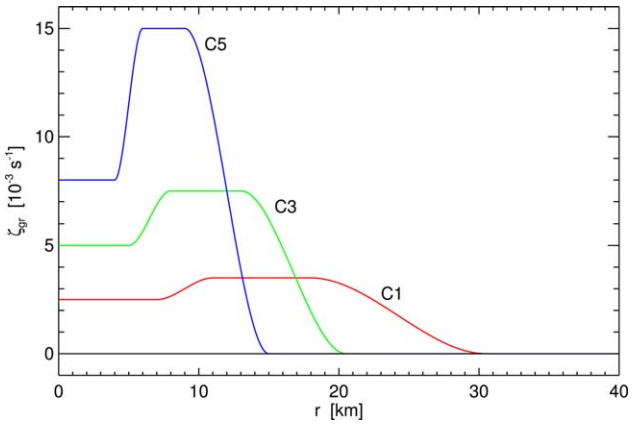

Figure 4. Radial profiles of $\zeta_{gr}(r)$ for the category 1, 3, and 5 cases having the parameter values listed in Table 1.

$$\zeta_{gr}(r)=\begin{cases}\zeta_0 & 0\le r\le r_1\\ \zeta_0 S\left(\dfrac{r-r_1}{r_2-r_1}\right) & \\ \quad+\zeta_1 S\left(\dfrac{r_2-r}{r_2-r_1}\right) & r_1\le r\le r_2\\ \zeta_1 & r_2\le r\le r_3\\ \zeta_1 S\left(\dfrac{r-r_3}{r_4-r_3}\right) & r_3\le r\le r_4\\ 0 & r_4\le r<\infty\end{cases}, \tag{14}$$

where $r_1, r_2, r_3, r_4, \zeta_0$, and ζ_1 are specified constants, and $S(s)=1-3s^2+2s^3$ is an interpolating function satisfying $S(0)=1, S(1)=0$, and $S'(0)=S'(1)=0$. Figures 4 and 5 show $\zeta_{gr}(r)$ and $v_{gr}(r)$ profiles for the three vortices with the parameter values listed in Table 1. The maximum values of the gradient wind $v_{gr}(r)$ for the category 1, 3, and 5 cases are 37.5, 55, and 75 m s^{-1}, respectively. For each case the radial derivative of $\zeta_{gr}(r)$ has both signs, so the Rayleigh necessary condition for barotropic instability is satisfied. However, in each case, the width of the annular region of high vorticity is larger than the radius of the region of low central vorticity (i.e., these are thick annular rings). A detailed linear

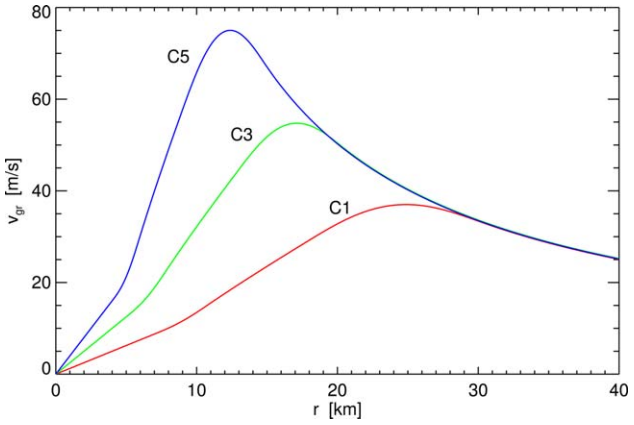

Figure 5. Radial profiles of $v_{gr}(r)$ for the category 1, 3, and 5 cases having the parameter values listed in Table 1.

Table 1. Initial Condition Parameters for Vortices in Figures 4 and 5[a]

Case	r_1 (km)	r_2 (km)	r_3 (km)	r_4 (km)	ζ_0 ($\times 10^{-3}$ s^{-1})	ζ_1 ($\times 10^{-3}$ s^{-1})
C1	7	11	18	30.5	2.5	3.5
C3	5	8	13	20.5	5.0	7.5
C5	4	6	9	15	8.0	15.0

[a]Numerical values of the gradient wind parameters $r_1, r_2, r_3, r_4, \zeta_0$, and ζ_1 for the category 1, 3, and 5 vortices.

analysis [*Schubert et al.*, 1999, Figures 1 and 2] and numerical experiments with a nonlinear model [*Hendricks et al.*, 2009, Figure 5] show that such thick rings are exponentially stable.

[14] Figure 6 shows the time evolution of the boundary layer flow beneath the category 3 vortex. The four plots of Figure 6 show radial profiles ($0 \le r \le 40$ km) of the boundary layer radial wind u, tangential wind v, vertical velocity w, and relative vorticity ζ, with the five curves in each plot for times 0, 0.5, 1.0, 2.0, and 3.0 h. The initial boundary layer flow (dashed curves) has $u = 0$ and v equal to the gradient wind. Note that strong radial inflow, supergradient/subgradient tangential winds, large boundary layer pumping, and large relative vorticity quickly develop, with the establishment of a near steady state by 2 or 3 h. Due to the $u(\partial u/\partial r)$ term in the radial equation of motion, a shock-like structure develops a few kilometers inside the radius of maximum gradient wind. The maximum radial inflow is approximately 22 m s^{-1}. Near the shock radius this radial inflow decreases inward to zero over a narrow radial interval, thereby producing an intense, narrow spike in the boundary layer pumping.

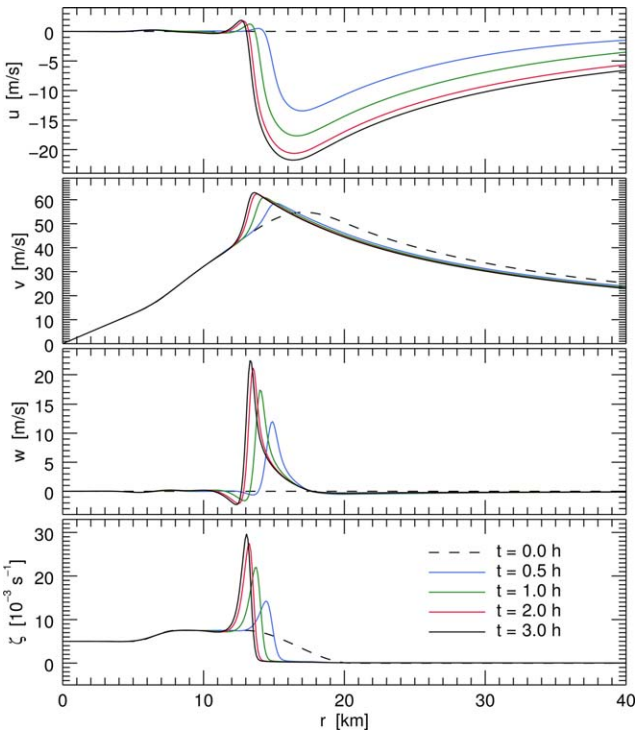

Figure 6. Slab boundary layer model results for the category 3 forcing case. The four plots show the boundary layer radial velocity $u(r,t)$, tangential velocity $v(r,t)$, vertical velocity $w(r,t)$, and relative vorticity $\zeta(r,t)$ for the inner region $0 \le r \le 40$ km. The results at the five different times t=0,0.5,1.0,2.0, and 3.0 h are indicated by the color coding. Initially, u=0,v=v_{gr},w=0, and $\zeta=\zeta_{gr}$. Radial inflow velocities exceeding 21 m s^{-1} quickly develop, and shock-like structures form in the region $13 \le r \le 15$ km, leading to vertical velocities exceeding 22 m s^{-1}. A near steady state is reached within 2 or 3 h, with the boundary layer tangential wind becoming supergradient in the region $12 < r < 16$ km and subgradient in the region $r > 16$ km.

[15] The category 1 and 5 vortices also quickly evolve into a near steady state, with small changes after 2 or 3 h. For comparison, Figure 7 shows u, v, w, and ζ for $t = 0$ and $t = 3$ h for each category vortex. An interesting feature of the radial profiles of $w(r,t)$ is the very sharp gradient on the inner side and the relatively slower decrease on the outer side of the maximum. Through the mass continuity equation (3), this behavior of $w(r,t)$ is related to the shock-like structure of $u(r,t)$. To a certain extent the radial structure of $w(r,t)$ in the slab model agrees with the observed radial structure of the red curve in the lower plot of Figure 1, which also shows a weaker gradient on the outside edge of the maximum. Another interesting feature of the category 3 and 5 cases is the rather large boundary layer pumping that the slab model produces, when compared with the

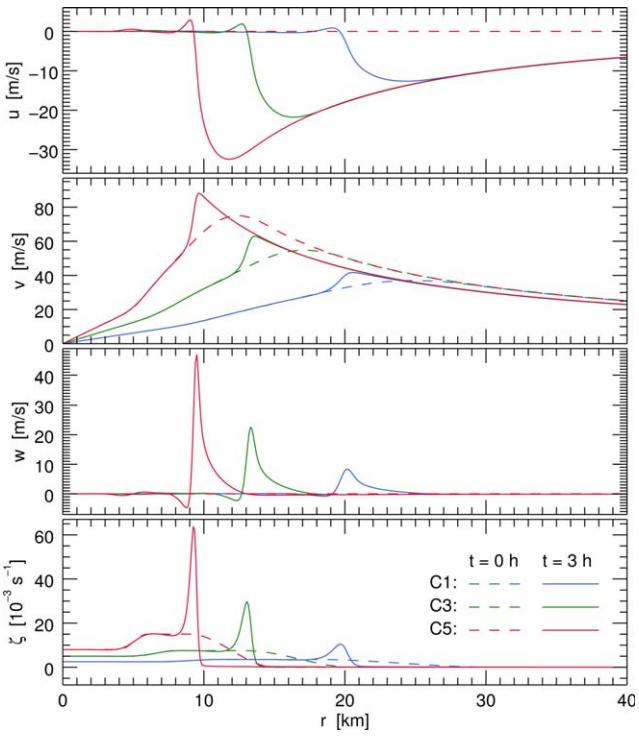

Figure 7. Steady-state (i.e., $t = 3$ h) slab boundary layer model results for the C1, C3, and C5 forcing cases.

observations of Figure 1. Some of this discrepancy is probably due to the simplicity of the slab model and the chosen value of K, but some may be explained by the low elevation of the flight level for the red curve in the lower plot of Figure 1, i.e., there may have been radially convergent flow above flight level so that a larger w might have been measured if the aircraft had flown several hundred meters higher. In actual hurricanes, this shock effect makes the inner core boundary layer a dangerous place for research aircraft. The location of shock formation also plays a crucial role in determining the eyewall radius, and hence where the diabatic heating will occur, relative to the region of high inertial stability.

[16] One of the important assumptions in the formulation of the slab boundary layer model (1)–(6) is that h is a constant. To assess the consequences of different choices of this constant, we have run the slab model with case C3 forcing for the five choices h=500, 750, 1000, 1250, and 1500m. The resulting "steady-state" (i.e., $t = 3$ h) radial profiles of u, v, w, and ζ are shown in Figure 8. The deepest boundary layer ($h = 1500$ m) produces a maximum inflow of 18 m s^{-1}, shock-like features at $r \approx 14$ km, and a maximum boundary layer pumping (i.e., w at $z = 1500$ m) of 27.5 m s^{-1}, while the shallowest boundary layer ($h = 500$ m) produces a maximum inflow of 29 m s^{-1}, shock-like features at $r \approx 11.5$ km, and a maximum boundary layer pumping (i.e., w at $z = 500$ m) of 15 m s^{-1}. In boundary layer models that have high resolution in both the vertical and radial directions, the boundary layer depth becomes shallower in the vortex core where the inertial stability is larger [*Kepert*, 2001]. Thus, while the constant depth slab model can serve as a basis for qualitative and semiquantitative understanding, accurate simulation of the shock location and structure is best obtained with more general models that include high vertical and horizontal resolution.

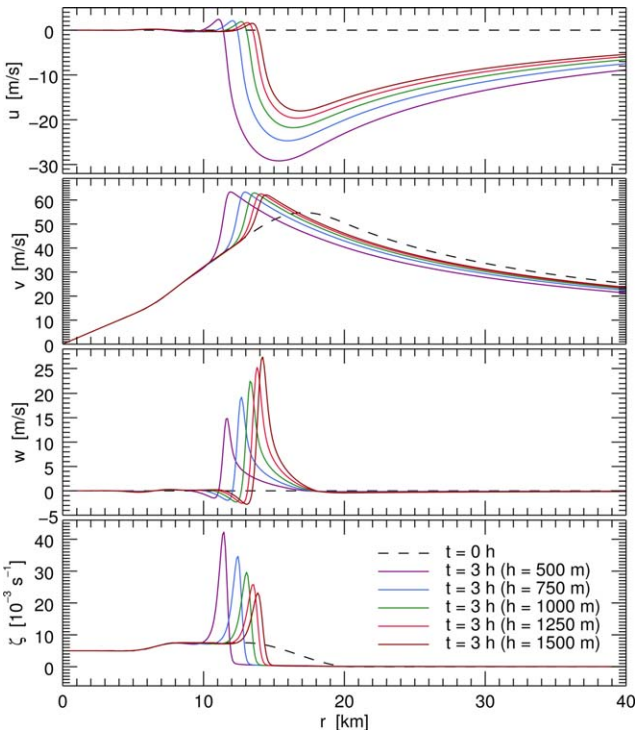

Figure 8. Steady-state (i.e., $t = 3$ h) slab boundary layer model results for the C3 forcing case with the five different assumed boundary layer depths h=500,750,1000,1250, and 1500 m. The third plot shows the radial profile of $w = -h[\partial(ru)/r\partial r]$ at $z = h$, so that even though the $h = 500$ m case has the strongest inflow, it has the weakest vertical velocity at $z = h$.

[17] We can also obtain a Lagrangian interpretation of the model results by writing the original equations (1) and (2) in the form

$$\frac{du}{dt} = -\left(\frac{w^- + c_D U}{h}\right)u + \left(f + \frac{v + v_{gr}}{r}\right)(v - v_{gr}) + K\frac{\partial}{\partial r}\left(\frac{\partial(ru)}{r\partial r}\right), \tag{15}$$

$$\frac{d\left(rv + \frac{1}{2}fr^2\right)}{dt} = -\left(\frac{w^- r(v - v_{gr}) + c_D U r v}{h}\right) + Kr\frac{\partial}{\partial r}\left(\frac{\partial(rv)}{r\partial r}\right), \tag{16}$$

where $(d/dt) = (\partial/\partial t) + u(\partial/\partial r)$ is the derivative following the boundary layer radial motion, i.e., the derivative along lines defined by

$$\frac{dr}{dt} = u. \tag{17}$$

In regions where $w \geq 0$, the w^- terms in equations (15) and (16) vanish, and the lines defined by equation (17) are the characteristics of the hyperbolic system that results from the neglect of the horizontal diffusion terms in equations (15) and (16). However, in regions where w^- does not vanish, these w^- terms need to be expressed in terms of $(\partial u/\partial r) + (u/r)$, and then the $\partial u/\partial r$ parts need to be brought over to the left-hand sides of equations (15) and (16), thereby making the calculation of characteristics somewhat more involved and leading to the presence of another set of characteristics, in addition to those obtained from equation (17). For simplicity, the present discussion is limited to trajectories, as defined by equation (17), rather than a full analysis of both sets of characteristics.

[18] The trajectories in the (r,t)-plane were computed by numerical integration of equation (17) using the same 1 s time step used for the numerical solution of equations (1) and (2). These trajectories are shown for the forcing case C3 in the three plots of Figure 9, along with isolines of the radial velocity u (top), the tangential velocity v (middle), and the absolute angular momentum $m = rv + \frac{1}{2}fr^2$ (bottom). A blowup of these trajectories, for the region $10 \leq r \leq 20$ km, is shown in Figure 10, along with isolines of the boundary layer pumping w (top) and the relative vorticity ζ (bottom). Since $u = 0$ initially, all the trajectory curves are vertical in the (r,t)-plane at $t = 0$. Since the radial flow inside $r \approx 13$ km remains weak, all the trajectory curves remain nearly

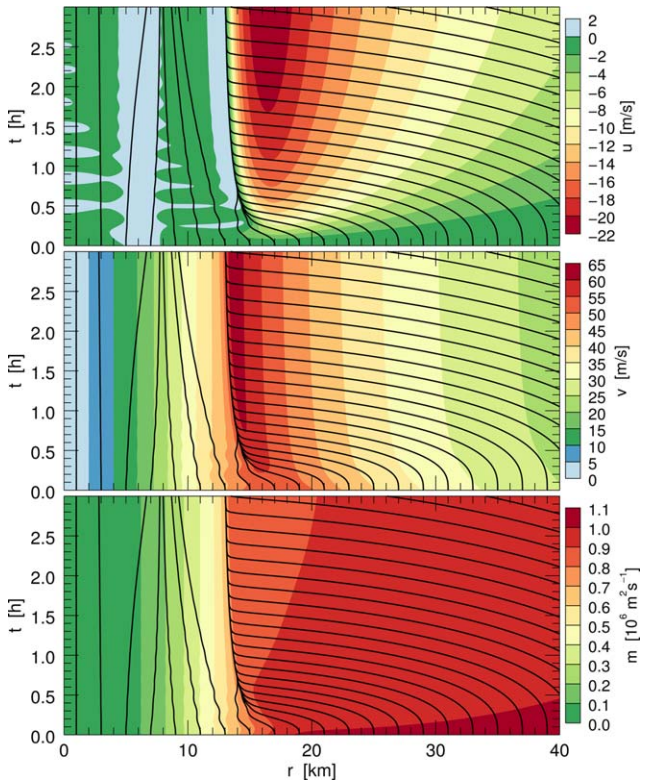

Figure 9. Trajectory curves in the (r,t)-plane for forcing case C3 are shown in the three plots, along with isolines of (top) the radial velocity u, (middle) the tangential velocity v, and (bottom) the absolute angular momentum $m=rv+\frac{1}{2}fr^2$. Note the development of the shock-like structure in the interval $13\leq r\leq 15$ km.

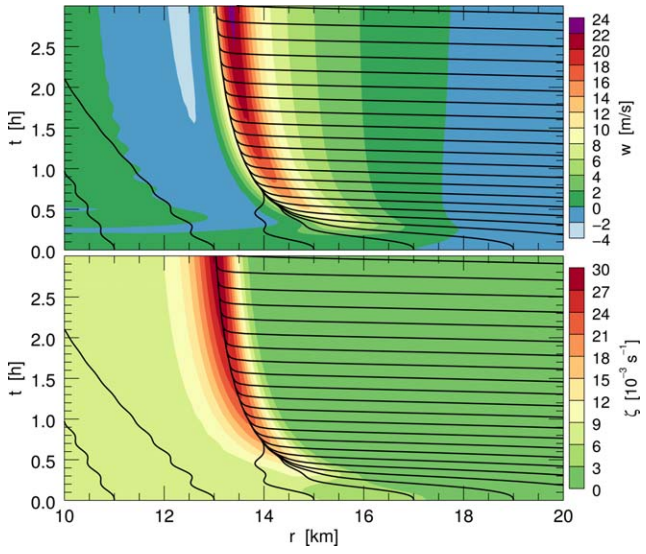

Figure 10. Trajectory curves in the (r,t)-plane for forcing case C3 are shown in the two plots, along with isolines of (top) the vertical velocity w and (bottom) the relative vorticity ζ. Note that this is a blowup ($10\leq r\leq 20$ km) of the shock-like region shown in Figure 9.

vertical inside this radius. Outside $r\approx 15$ km the trajectories quickly turn inward as a near steady state is established by $t=2$ h. By $t=0.5$ h the inward turning trajectories have established a shock-like structure at $r=15$ km. This structure moves slowly inward to $r=13$ km during the interval $0.5\leq t\leq 3$ h.

[19] To interpret Figure 9 in terms of equations (15) and (16), we first note that the horizontal diffusion terms on the right-hand sides are small except near the shock. The first term on the right-hand side of equation (15) always damps u since $(w^{-}+c_D U)/h>0$. The second term on the right-hand side of equation (15) tends to be negative in outer regions where the boundary layer flow is subgradient ($v-v_{gr}<0$) and to be positive in inner regions where the boundary layer flow is supergradient ($v-v_{gr}>0$). Thus, in the subgradient region, the effect of the second term is to make $(du/dt)<0$, i.e., to make an inflowing parcel flow inward even faster. In the supergradient region, the effect of the second term is to make $(du/dt)>0$, i.e., to make an inflowing parcel slow down. However, it should be emphasized that although the $\left[f+\left(v+v_{gr}\right)/r\right]\left(v-v_{gr}\right)$ term can play a role in decelerating the inflow, the formation of a shock-like structure in u is primarily due to the Burgers' shock term $u(\partial u/\partial r)$, which is associated with intersecting characteristics and nearly discontinuous behavior in u. Similarly, as seen in the bottom plot of Figure 9, the first term on the right-hand side of equation (16) tends to damp the absolute angular momentum $m=rv+\frac{1}{2}fr^2$ along each trajectory. However, as shown in the middle plot of Figure 9, the behavior of v is quite different, showing a rapid increase on most of each inflowing trajectory. One way of understanding the simultaneous decrease in m and increase in v along an inflowing boundary layer trajectory is through the relation

$$r\frac{dv}{dt}=\frac{dm}{dt}-\left(f+\frac{v}{r}\right)ru. \tag{18}$$

Along inflowing trajectories in Figure 9, the $-[f+(v/r)]ru$ term is positive and typically five times as large as $|dm/dt|$, which means that $(dv/dt)>0$ even though $(dm/dt)<0$. The process is somewhat analogous to spinning ice skaters who are losing angular momentum through friction with the ice surface but still manage to spin faster by bringing in their arms at a rate that more than compensates for the frictional loss. In a hurricane, it is this process that allows the strongest tangential winds to occur in the frictional boundary layer. This view is consistent with that of *Smith et al.* [2009], who have emphasized the important role of gradient wind imbalance in the tropical cyclone boundary layer.

[20] The slab boundary layer model solutions shown in Figures 6–10 have a relatively smooth character because equations (1)–(6) constitute a filtered model in the sense that the pressure field is fixed, so there is no mutual adjustment of the pressure and wind fields through inertia-gravity wave radiation. In a more general model with such mutual pressure-wind adjustment, the fields would have a less-smooth character, more like the observed fields in Figure 1.

[21] With such strong boundary layer pumping, we would expect that the formation of a hurricane boundary layer shock could be dramatically imprinted on the radial structure of the equivalent potential temperature field above the boundary layer. An example from the 700 hPa flight-level data in Hurricane Rita (1937 UTC on 21 September 2005) was given by *Sitkowski et al.* [2012] as their Figure 3. With tangential winds of 75–80 m s^{-1}, a boundary layer shock had apparently formed in the lowest kilometer, with an intense spike in the boundary layer pumping just inside the radius of maximum wind. The high θ_e air pumped out of the boundary layer was imprinted on the radial profile of θ_e at 700 hPa, with localized θ_e anomalies of approximately 20 K near the radius of the boundary layer shock.

[22] *Eliassen and Lystad* [1977] developed a filtered theory of the turbulent boundary layer under a circular vortex. Their model filters toroidal inertia oscillations by neglecting the material derivative of u in the radial equation of motion. Since their approximation involves the neglect of the $u(\partial u/\partial r)$ term, the Burgers' shock effect is eliminated. However, their model still produces strong boundary layer pumping that maximizes away from the vortex axis. We have considered an approximation of the slab model (1)–(6) that has a certain similarity to the Eliassen-Lystad model. The approximate slab model consists of equations (1)–(6), but with the $u(\partial u/\partial r)$ term neglected in equation (1). The results of this approximate model have then been compared with the results of the unapproximated slab model. In general, the two models produce similar results except near the radius of maximum gradient wind, where they produce quite different fields. Although the approximate model can produce a rapid change in the radial velocity and a fairly strong updraft, this is not the same as the Burgers' shock effect, leading to the extreme behavior shown in the unapproximated model. When the $u(\partial u/\partial r)$ term is included, it becomes an important part of the radial momentum balance. Then, in the quasi-steady-state near the radius of maximum gradient wind, the primary balance in equation (1) is between the $u(\partial u/\partial r)$ term and the $\left[f+\left(v+v_{gr}\right)/r\right]\left(v-v_{gr}\right)$ term, so that $v-v_{gr}$ changes sign at essentially the same radius where $\partial u/\partial r$ changes sign. Although it provides a reasonable approximation away from the radius of maximum gradient wind, the approximate model does not provide a self-consistent approximation for all radii. The approximate solution is defective in the sense that it implies large values of the $u(\partial u/\partial r)$ term even though this term is neglected in the calculation. Thus, the inclusion of the $u(\partial u/\partial r)$ term is crucial for the accurate simulation of the location, shape, and strength of the boundary layer pumping.

4. Reinterpretation of Previous Observational and Modeling Studies

[23] The slab boundary layer model results presented here can serve as the basis for reinterpretation of many observational and modeling studies of tropical cyclones. For example, the observational study of *Barnes and Powell* [1995] can be reinterpreted as presenting evidence that boundary layer shocks can form at large radii, as when secondary eyewalls form. Their Hurricane Gilbert (1988) observations are reproduced here as Figures 11 and 12. Figure 11 shows the radar reflectivity of Gilbert at 1731 UTC, 12 September 1988, as the eye was making landfall on Jamaica. An outer band, located approximately 175 km southeast of the cyclone center, was repeatedly sampled by NOAA WP-3D aircraft flying 19 passes normal to the band at a variety of levels below approximately 1500 m. Storm-relative radial velocity and vertical velocity from one of these passes, taken at $z = 720$ m between 1722:00 and 1731:10 UTC near the thick line in Figure 11, are shown in the top and middle plots of Figure 12. Outside $r = 170$ km the storm-relative radial velocity is inward at approximately 15 m s^{-1}, but it rapidly decreases to nearly zero over a few kilometers radial distance. This strong convergence is associated with an updraft that exceeds 6 m s^{-1} at $z = 720$ m. Based on the 19 radial passes through the band, *Barnes and Powell* [1995] also constructed the composite radius-height cross section shown in the bottom plot of Figure 12. Note that the shock-like structure in the relative radial wind is most extreme near the surface but extends upward to 1500 m. For other examples of shock-like behavior in outer bands, the reader is referred to the observational studies of *Barnes et al.* [1983] and *Powell* [1990a, 1990b]. The wind structure shown in these studies is consistent with the notion that boundary layer shock-like structures can form at large radii and that they can be the primary control on the location and strength of the deep convection in secondary eyewalls and outer bands.

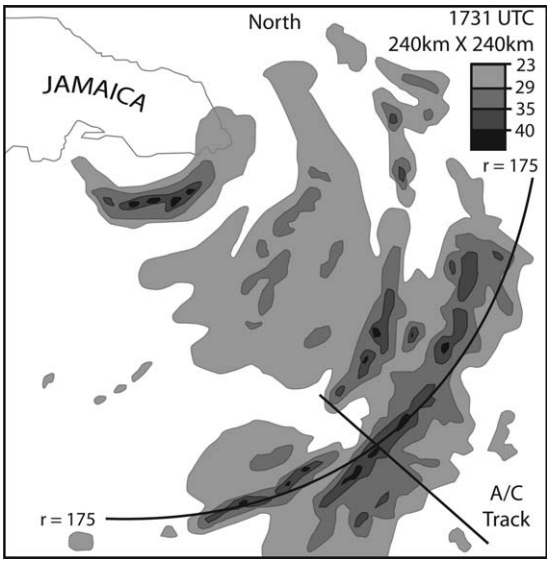

Figure 11. NOAA WP-3D lower fuselage radar reflectivity (dBZ) for Hurricane Gilbert at 1731 UTC, 12 September 1988, when its eye was making landfall on Jamaica. Nineteen boundary layer flight legs (see Figure 12) were made normal to the band located approximately 175 km southeast of the storm center. Reproduced from Figure 2 of *Barnes and Powell* [1995], ©American Meteorological Society, and used with permission.

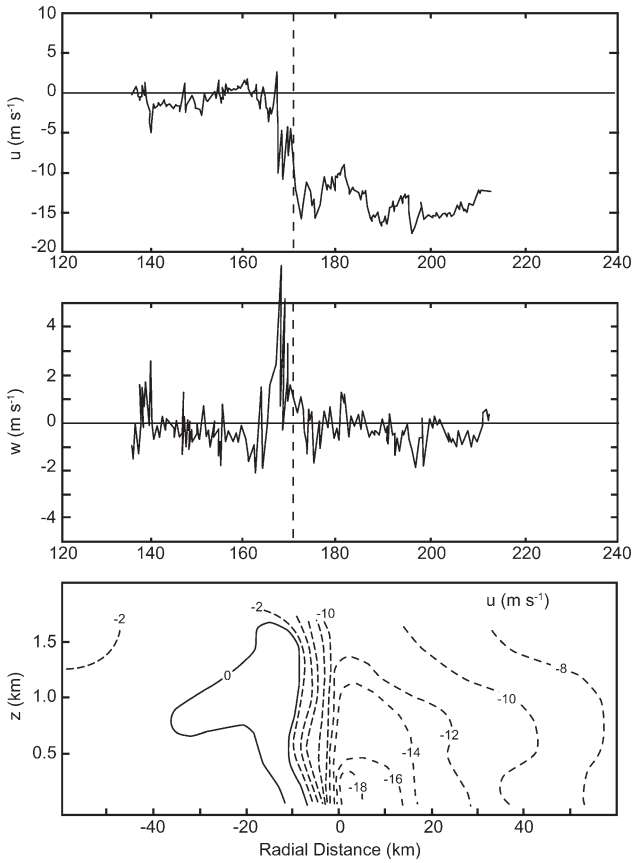

Figure 12. (top) Relative radial velocity and (middle) vertical velocity as measured by one of the NOAA WP-3D aircraft at $z = 720$ m from 1722:00 to 1731:10 UTC along the bold line in Figure 11. A boundary layer shock in the radial flow has developed at a radius of approximately 170 km, with an associated vertical velocity exceeding 6 m s^{-1}. (bottom) A composite radius-height cross section of the relative radial velocity, based on 19 flight legs normal to the band. Adapted from Figures 5a, 5c, and 6 of *Barnes and Powell* [1995], ©American Meteorological Society, and used with permission.

[24] It is also possible to reinterpret the results of numerical simulations of tropical cyclones with axisymmetric, nonhydrostatic, moist models. Such simulations were pioneered by *Yamasaki* [1977, 1983] and refined by *Willoughby et al.* [1984], *Nasuno and Yamasaki* [1997], *Hausman et al.* [2006], and *Mrowiec et al.* [2011]. These studies generally used horizontal and vertical grid spacing of approximately 500 m so that the simulations were "cloud-resolving" and did not involve parameterization of cumulus convection. A summary of one such numerical integration [*Yamasaki*, 1983] is reproduced here as Figures 13 and 14, which are time-radius sections of the surface rainfall intensity and the tangential wind at $z = 0.9$ km. Initially, the model atmosphere is at rest, with nine warm bubbles at low levels inside $r = 80$ km. During the first 80 h, the edge of the rainy area expands outward to $r = 220$ km, while the tangential wind slowly increases from zero to approximately 9 m s^{-1}. During the next 55 h, the edge of the rainy area contracts, with hurricane force tangential winds being produced at 134 h. Thereafter, rain in the core is suppressed and a quasi-steady eye-eyewall structure is established. By 144 h, what appears to be a strong boundary layer shock has formed, and the tangential wind has accelerated to approximately 80 m s^{-1}. The boundary layer shock-like structure at 144 h is clearly depicted in Figure 15, which shows a 50 m s^{-1} radial inflow decelerated to rest in the region $15 \leq r \leq 20$ km. Similar behavior occurs in the axisymmetric, nonhydrostatic simulations of *Hausman et al.* [2006, Figure 8] and *Mrowiec et al.* [2011, Figure 4b], both done with 500 m radial resolution in the inner core. For example, the simulations of *Hausman et al.* [2006] show the development of a 30 m s^{-1} near-surface radial inflow that decreases to zero over a radial interval of approximately 5 km, producing a narrow zone of 12 m s^{-1} boundary layer pumping near $r = 10$ km. This boundary layer pumping appears to control the location of the eyewall latent heat release through the entire troposphere, which results in a narrow vertical tower of high vorticity [*Hausman et al.*, 2006, Figure 10].

[25] Another interesting study, designed to clarify the role of surface friction in tropical cyclones, was performed by *Yamasaki* [1977], who ran the following three axisymmetric, nonhydrostatic model experiments: in case 1 the drag coefficient was held constant at 2.5×10^{-3}; in case 2 the drag coefficient was set to zero; in case 3 the drag coefficient was zero for the first 24 h, was then linearly increased to 2.5×10^{-3} over the period from 24 to 36 h, and was subsequently held fixed at this value. These experiments are summarized in Figure 16, which shows the eye radius (dashed lines) and the outer radius of the convective area (solid lines). In case 1, an eye-eyewall structure develops, with the eyewall in the annular region $2 \leq r \leq 15$ km. In case 2, an eye-eyewall structure does not develop. In case 3, as the drag coefficient is increased, the storm transitions into a structure similar to case 1, with the eyewall in the annular region $8 \leq r \leq 22$ km. A cross section of the radial velocity, averaged from 36 to 48 h for case 2, is shown in the bottom plot of Figure 17. At this stage the maximum tangential wind is approximately 14 m s^{-1}, and there is weak radial inflow of 1–2 m s^{-1} over the lower half of the troposphere. In contrast, a cross section of the radial velocity, averaged from 60 to 72 h for case 3, is shown in the top plot of Figure 17. In this case, the maximum tangential wind is approximately 40 m s^{-1}, and there is strong radial inflow ($\sim$20 m s^{-1}) in the boundary layer, with a shock-like structure having formed just outside 10 km radius. These modeling results are consistent with the idea that eye-eyewall structure is intimately related to the formation of a boundary layer shock-like structure in the radial velocity.

[26] In recent years, remarkable progress has been made in the numerical simulation of secondary eyewall formation and concentric eyewall cycles using 3-D

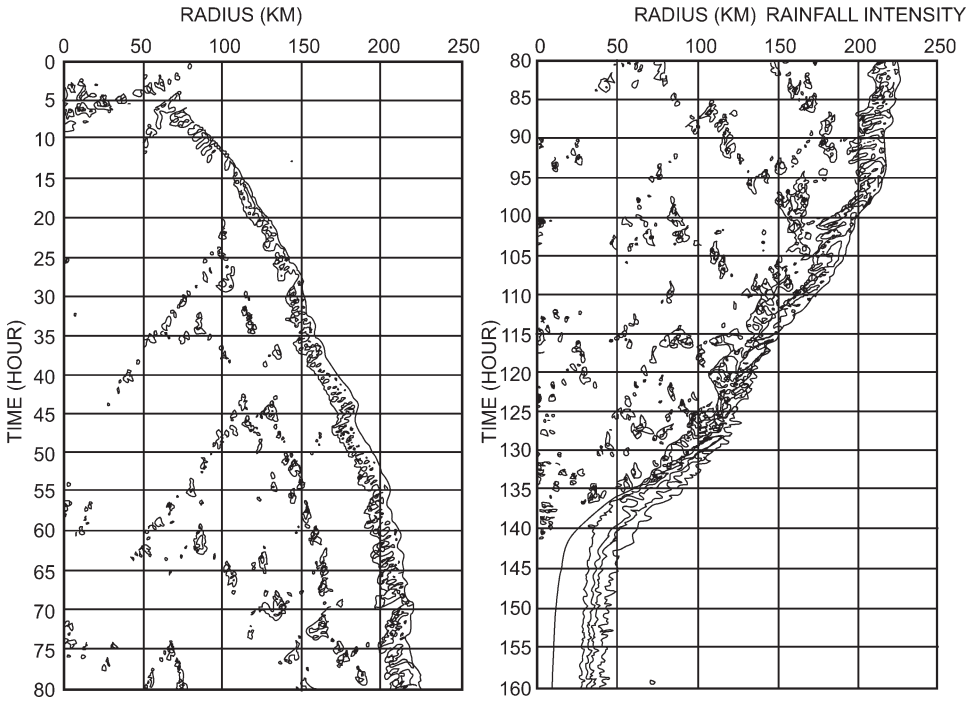

Figure 13. Time-radius section of surface rainfall intensity (isolines are for 1, 5, 10, and 20 mm/10 min) for a numerical experiment performed by *Yamasaki* [1983] using an axisymmetric nonhydrostatic model. The eye-eyewall structure emerges at approximately 140 h, with the rainfall gradient on the inner edge of the eyewall being so strong that the four isohyets are indistinguishable. Reproduced from Figure 1 of *Yamasaki* [1983], and used with permission.

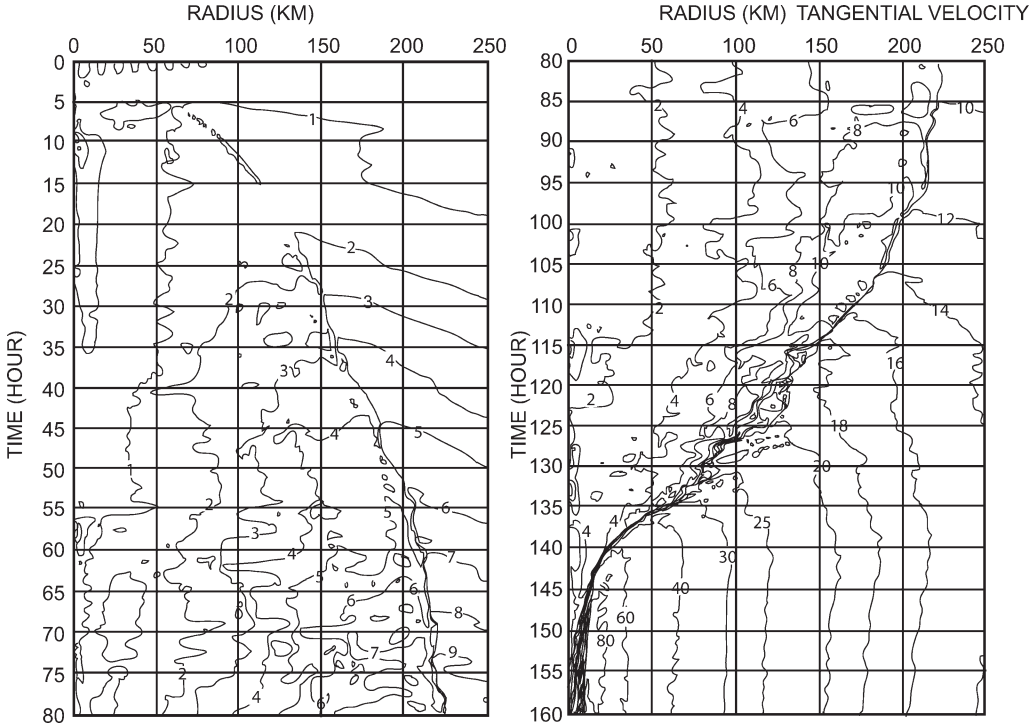

Figure 14. Time-radius section of the tangential wind (m s^{-1}) at z=0.9 km for the same numerical experiment shown in Figure 13, as performed by *Yamasaki* [1983]. Note the variable contour interval. Hurricane force tangential winds occur at t = 134 h, after more than 24 h of contraction. During the next 10 h the classic eye-eyewall structure emerges, and the vortex rapidly intensifies to 80 m s^{-1}. Reproduced from Figure 2 of *Yamasaki* [1983], and used with permission.

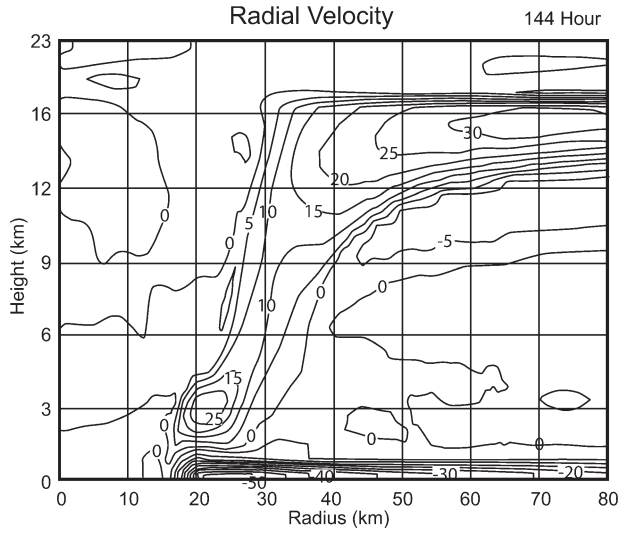

Figure 15. Vertical cross section of radial velocity (m s^{-1}) at 144 h, soon after the classic eye-eyewall structure has emerged in the axisymmetric numerical model of *Yamasaki* [1983]. A strong boundary layer shock has formed just outside $r = 15$ km, with an associated vertical velocity (not shown) of 12 m s^{-1} at z=1.5 km. Adapted from Figure 8a of *Yamasaki* [1983] and used with permission.

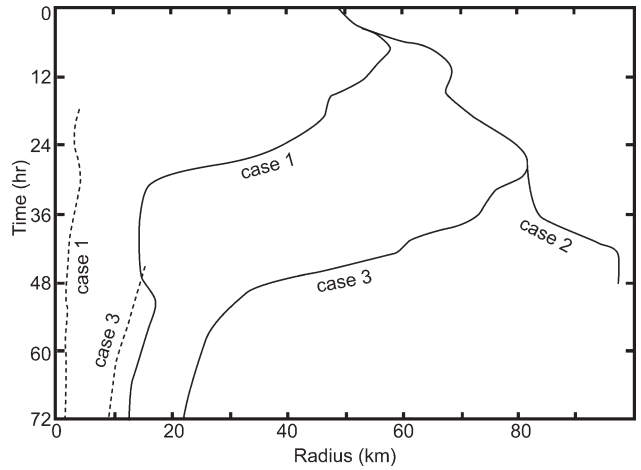

Figure 16. Eye radius (dashed lines) and outer radius of the convective area (solid lines) for three numerical experiments performed by *Yamasaki* [1977] using an axisymmetric, nonhydrostatic hurricane model. Case 1 (c_D=2.5×10^{-3}) develops an eye-eyewall structure, with the eyewall in the annular region $2 \leq r \leq 15$ km. Case 2 (c_D=0) does not develop an eye-eyewall structure. After c_D is increased from zero to 2.5×10^{-3} between 24 and 36 h, case 3 also develops an eye-eyewall structure, with the eyewall in the annular region $8 \leq r \leq 22$ km. Adapted from Figure 2 of *Yamasaki* [1977] and used with permission.

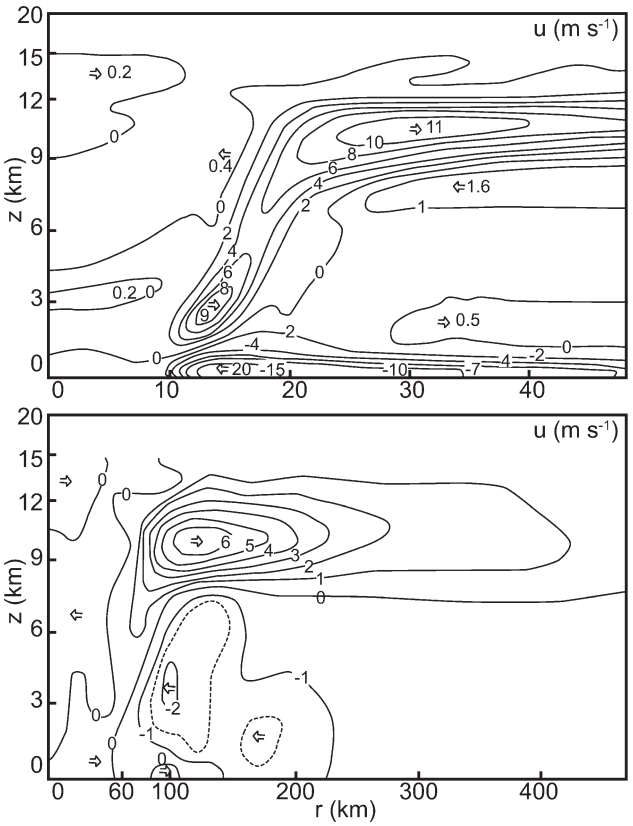

Figure 17. (bottom) Vertical cross section of radial velocity, averaged from 36 to 48 h, for Yamasaki's case 2. Since case 2 has c_D=0, there is no concentrated boundary layer inflow, but rather a weak inflow of 1–2 m s^{-1} in the lower half of the troposphere due to diabatic processes. (top) A similar cross section (but note the different horizontal scale) for Yamasaki's case 3, averaged from 60 to 72 h. In case 3 a boundary layer shock in the radial flow has developed just outside a radius of approximately 10 km, with an associated vertical velocity (not shown) exceeding 6 m s^{-1} at a height of 1 km. Adapted from Figures 5b and 8b of *Yamasaki* [1977] and used with permission.

models [*Houze et al.*, 2007; *Terwey and Montgomery*, 2008; *Wang*, 2008, 2009; *Zhou and Wang*, 2009; *Judt and Chen*, 2010; *Abarca and Corbosiero*, 2011; *Martinez et al.*, 2011; *Zhou and Wang*, 2011; *Rozoff et al.*, 2012; *Wu et al.*, 2012; *Huang et al.*, 2012; *Menelaou et al.*, 2012; *Lee and Chen*, 2012; *Chen and Zhang*, 2013]. These simulations, although obviously at much larger horizontal grid spacings than the present axisymmetric slab model, can be interpreted as demonstrating the importance of the boundary layer shock phenomenon. For example, one illuminating simulation by *Rozoff et al.* [2012, Figure 2d] shows that the destruction of the inner eyewall is closely associated with the development of a secondary eyewall shock-like structure at larger radius. Simulations such as theirs are supportive of the notion that the fundamental interaction between concentric eyewalls occurs through the boundary layer and takes the

form of a control and an ultimate destruction of the inner eyewall by the outer eyewall boundary layer shock.

5. Concluding Remarks

[27] The structure of the boundary layer wind field in Hurricane Hugo (1989) has been interpreted in terms of an axisymmetric slab boundary layer model. The 20 m s^{-1} vertical velocity in the boundary layer of Hugo has been explained by dry dynamics, i.e., by the formation of a shock in the boundary layer radial inflow, with very small radial flow on the inside edge of the shock and large radial inflow on the outside edge of the shock. Shock formation is associated with the $u(\partial u/\partial r)$ term in the radial momentum equation. Since u is an order of magnitude larger in the boundary layer than in the overlying fluid (approximately 20 m s^{-1} versus 2 m s^{-1}), shocks are primarily a phenomenon of the boundary layer. The development of a shock in the boundary layer radial wind u leads to a shock in the boundary layer tangential wind v since $\partial v/\partial t = -(f+\zeta)u + \cdots$, with large inflow ($u < 0$) producing large $\partial v/\partial t$ on the outside edge of the shock. A thin sheet of very high vorticity develops in the boundary layer, and it may extend upward due to vertical advection. Horizontal diffusion has been used here to avoid multivalued solutions near the shock. Although horizontal diffusion is a simple and effective way to avoid this problem, it is not the only way. Two alternatives are shock-tracking methods, in which the governing PDEs are supplemented by jump conditions across discontinuities, or shock-capturing methods such as those used in the Fortran routines of the Conservation Law Package (CLAWPACK) described by *Leveque* [2002].

[28] For the boundary layer structures simulated here, we have chosen to use the terms "boundary layer shock" or "Burgers' shock," rather than the terms "bore" or "front." Our assumption of constant h obviously precludes the development of jumps in the boundary layer depth, so use of the term "bore" would be confusing. In addition, we have chosen to reserve the term "front" for structures that arise not from $u(\partial u/\partial r)$, but rather from the combination of $u(\partial v/\partial r), w(\partial v/\partial z)$, $u(\partial\theta/\partial r)$, and $w(\partial\theta/\partial z)$, with the rotational flow v and the potential temperature θ being related by the gradient form of thermal wind balance. However, it should be noted that this distinction is not completely sharp, since the "boundary layer shocks" studied here depend not only on the $u(\partial u/\partial r)$ term in the radial equation of motion but also on the $u(\partial v/\partial r)$ term (or more generally on the $(f+\zeta)u$ term) in the tangential equation of motion, which leads to the shock-like structure in the v field. Even with this caveat, it is helpful to use terminology that distinguishes features that can be accurately modeled using the gradient balance assumption (i.e., fronts) from features that cannot be modeled using gradient balance (i.e., boundary layer shocks).

[29] For an axisymmetric, nontranslating pressure field, the boundary layer shock is circular. If the pressure field translates, the shock becomes asymmetric. The low azimuthal wave number aspects of this problem were studied by *Shapiro* [1983]. It would be interesting to repeat his numerical experiments at much higher azimuthal resolution in order to more accurately simulate the dynamics of asymmetric shocks. Such simulations, using a different numerical model, have recently been described by *Williams* [2012].

[30] The slab boundary layer model described in section 2 can be regarded as a model that is at or near the bottom of a hierarchy of boundary layer models of increasing complexity. As discussed by *Kepert* [2010a, 2010b], the constant depth slab model does not capture certain important features found in height-resolving models [*Montgomery et al*., 2001; *Kepert*, 2001; *Kepert and Wang*, 2001] of the tropical cyclone boundary layer, e.g., the shallow boundary layer depth found near the cyclone core and the outward radial flow just above the boundary layer. However, the constant depth slab model does appear to capture the essence of the shock structure in the radial inflow and its consequences for boundary layer pumping and subgradient/supergradient behavior in the tangential wind.

[31] The phenomenon of boundary layer shocks puts demanding horizontal resolution requirements on 3-D full-physics tropical cyclone models. These horizontal resolution requirements are as strict or even stricter than those for accurate simulation of moist convection. For nested models, these requirements extend outward at least as far as typical radii for the formation of secondary eyewalls and outer spiral bands. In view of the importance of boundary layer shocks in determining the location of diabatic heating, accurate intensity forecasts probably require accurate simulations of such fine-scale aspects of the boundary layer.

[32] Finally, we reiterate the conclusion that a boundary layer shock is one of the essential ingredients of a hurricane vortex with a well-defined eyewall updraft structure. In fact, it could be said that the formation of a boundary layer shock is one of the most significant events in the life cycle of a hurricane, for it imposes on the storm a classic eye-eyewall structure.

Appendix A: Derivation of the Boundary Layer Equations

[33] The logical starting point in the derivation of equation (2) is the conservation relation for the absolute angular momentum $m = rv + \frac{1}{2}fr^2$. This conservation relation can be written in the flux form:

$$\frac{\partial(hm)}{\partial t} + \frac{\partial(ruhm)}{r\partial r} + mw^{+} - m_{\mathrm{gr}}\, w^{-} + c_D U r v = \frac{\partial}{r\partial r}\left(hKr^3 \frac{\partial}{\partial r}\left(\frac{v}{r}\right)\right), \tag{A1}$$

where $w^{+} = \frac{1}{2}(|w| + w)$ is the rectified boundary layer pumping, and $w^{-} = \frac{1}{2}(|w| - w)$ is the rectified boundary layer suction. According to equation (A1), there are five processes that can cause local time changes in the boundary layer absolute angular momentum: (i) radial divergence of the radial advective flux; (ii) upward flux

of m when $w > 0$, in which case $w^+ = |w|$ and $w^- = 0$; (iii) downward flux of m_{gr} when $w < 0$, in which case $w^+ = 0$ and $w^- = |w|$; (iv) loss of m through surface drag; and (v) radial divergence of the radial diffusive flux. To convert equation (A1) into a more convenient form, we differentiate the second term as a product of *ruh* and m and then make use of the continuity equation (3) to obtain equation (2).

[34] The derivation of the radial momentum equation (1) proceeds in a similar fashion. The flux form is

$$\frac{\partial(hu)}{\partial t} + \frac{\partial(ruhu)}{r\partial r} + uw^+ - h\left(f + \frac{v}{r}\right)v + \frac{h}{\rho}\frac{\partial p}{\partial r} + c_D U u = \frac{\partial}{r^2 \partial r}\left(hKr^3 \frac{\partial}{\partial r}\left(\frac{u}{r}\right)\right). \tag{A2}$$

Note that we have assumed the radial flow in the region above the boundary layer is very small, so that equation (A2) does not contain a term analogous to the $m_{gr} w^-$ term in equation (A1). The radial pressure gradient force in the boundary layer is now assumed to be equal to the radial pressure gradient force in the region above the boundary layer, where gradient balance exists. Thus, we can write

$$\left(f + \frac{v_{gr}}{r}\right)v_{gr} = \frac{1}{\rho}\frac{\partial p}{\partial r}, \tag{A3}$$

where the gradient wind $v_{gr}(r)$ is a specified function. To convert equation (A2) into a more convenient form, we differentiate the second term as a product of *ruh* and u and then make use of the continuity equation (3) and the relation (A3) to obtain equation (1).

Appendix B: Horizontal Diffusivity

[35] The Courant-Friedrichs-Lewy condition associated with the horizontal diffusion terms sets the stability constraint $K\Delta t/(\Delta r)^2 \lesssim 2/3$, so that for $\Delta r = 100$ m and $\Delta t = 1$ s, we must have $K \lesssim 6666$ m^2 s^{-1}. In order to determine an appropriate value of K, a series of numerical experiments were performed using $\Delta r = 100$ m, $\Delta t = 1$ s, and $K = 500, 1000, 1500, 2000,$ and 2500 m^2 s^{-1}. The results of these experiments (Figure 18) show that the steady-state (i.e., $t = 3$ h) radial profiles of u, v, w, and ζ are nearly identical, except near the shock, for these five values of K. As K decreases, there is a sharpening of the shock-like structure of u and v and an upward extension of the singular-like structure of w and ζ. This behavior is consistent with the idea that with infinitesimally small Δr and Δt, the limit $K \to 0$ leads to discontinuities in u and v and singularities in w and ζ. However, it should be noted that with finite, fixed values of Δr and Δt, the use of smaller and smaller values of K can result in unphysical spatial oscillations of the fields, i.e., the horizontal diffusion is not strong enough to regularize the solution, leading to oscillations of the type discovered by *Smith* [2003] and *Smith and Vogl* [2008]. Based on this numerical experience, we have chosen $K = 1500$ m^2 s^{-1} in all the experiments discussed in section 3.

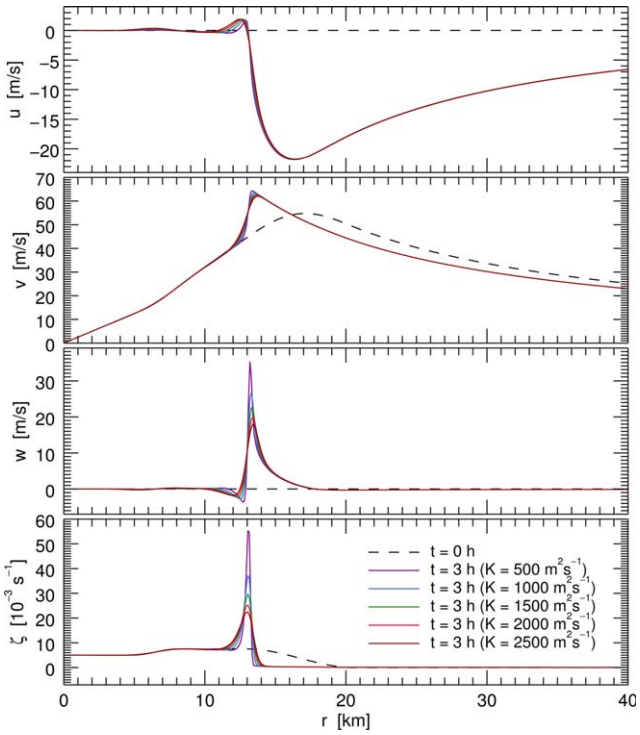

Figure 18. Initial (dashed) and steady-state (i.e., $t = 3$ h) radial profiles of u, v, w, and ζ for the category 3 forcing case and for the five different horizontal diffusivity values $K = 500, 1000, 1500, 2000,$ and 2500 m^2 s^{-1}. Note that smaller values of K result in a sharper shock-like structure for u and v and a sharper spike in w and ζ.

Since the purpose of the horizontal diffusion terms in the model is primarily to provide a degree of regularity to the numerical solution, there is no reason to consider a larger value of K. A slightly smaller value could have been chosen, but this would only have made the shock-like structure even more striking in the model results. In passing, we note that the value $K = 1500$ m^2 s^{-1} is consistent with the observational findings of *Zhang and Montgomery* [2012] for the boundary layer in the eyewall region of intense hurricanes.

[36] **Acknowledgments.** We would like to thank Paul Ciesielski, Mark DeMaria, Greg Holland, Jeff Kepert, Eric Maloney, Kate Musgrave, Chris Slocum, Sue van den Heever, Hugh Willoughby, and two anonymous reviewers for their advice. This research has been supported by the National Science Foundation under grant ATM-0837932 and under the Science and Technology Center for Multi-Scale Modeling of Atmospheric Processes, managed by Colorado State University through cooperative agreement ATM-0425247, and by the National Oceanographic Partnership Program through ONR contracts N00014-10-1-0145 and N00014-08-1-0250. The calculations were made on high-end Linux workstations generously provided through a gift from the Hewlett-Packard Corporation.

References

Abarca, S. F., and K. L. Corbosiero (2011), Secondary eyewall formation in WRF simulations of Hurricanes Rita and Katrina (2005), *Geophys. Res. Lett.*, *38*, L07802, doi:10.1029/2011GL047015.

Andreas, E. L., L. Mahrt, and D. Vickers (2012), A new drag relation for aerodynamically rough flow over the ocean, *J. Atmos. Sci.*, *69*, 2520–2537.

Anthes, R. A. (1971), Iterative solutions to the steady-state axisymmetric boundary-layer equations under an intense pressure gradient, *Mon. Weather Rev.*, *99*(4), 261–268.

Barnes, G. M., and M. Powell (1995), Evolution of the inflow boundary layer of Hurricane Gilbert (1988), *Mon. Weather Rev.*, *123*(8), 2348–2368.

Barnes, G. M., E. J. Zipser, D. Jorgensen, and F. Marks Jr. (1983), Mesoscale and convective structure of a hurricane rainband, *J. Atmos. Sci.*, *40*(9), 2125–2137.

Bender, M. A., I. Ginis, R. E. Tuleya, B. Thomas, and T. Marchok (2007), The operational GFDL coupled hurricane-ocean prediction system and a summary of its performance, *Mon. Weather Rev.*, *135*(12), 3965–3989.

Burgers, J. M. (1948), A mathematical model illustrating the theory of turbulence, *Adv. Appl. Mech.*, *1*, 171–199.

Chen, H., and D.-L. Zhang (2013), On the rapid intensification of Hurricane Wilma (2005). Part II: Convective bursts and the upper-level warm core, *J. Atmos. Sci.*, *70*, 146–172.

Chow, S. (1971), A study of the wind field in the planetary boundary layer of a moving tropical cyclone, M.S. thesis, 59 pp., Dep. of Meteorol. and Oceanogr., New York Univ., New York.

Cole, J. D. (1951), On a quasi-linear parabolic equation occurring in aerodynamics, *Q. Appl. Math.*, *9*, 225–236.

Donelan, M. A., B. K. Haus, N. Reul, W. J. Plant, M. Stiassnie, H. C. Graber, O. B. Brown, and E. S. Saltzman (2004), On the limiting aerodynamic roughness of the ocean in very strong winds, *Geophys. Res. Lett.*, *31*, L18306, doi:10.1029/2004GL019460.

Eliassen, A., and M. Lystad (1977), The Ekman layer of a circular vortex: A numerical and theoretical study, *Geophys. Norv.*, *31*, 1–16.

Emanuel, K. A. (1997), Some aspects of hurricane inner-core dynamics and energetics, *J. Atmos. Sci.*, *54*(8), 1014–1026.

Emanuel, K. A. (2003), A similarity hypothesis for air-sea exchange at extreme wind speeds, *J. Atmos. Sci.*, *60*(11), 1420–1428.

Haus, B. K., D. Jeong, M. Donelan, J. A. Zhang, and I. Savelyev (2010), Relative rate of sea-air heat transfer and frictional drag in very high winds, *Geophys. Res. Lett.*, *37*, L07802, doi:10.1029/2009GL042206.

Hausman, S. A., K. V. Ooyama, and W. H. Schubert (2006), Potential vorticity structure of simulated hurricanes, *J. Atmos. Sci.*, *63*(1), 87–108.

Hendricks, E. A., W. H. Schubert, R. K. Taft, H. Wang, and J. P. Kossin (2009), Life cycles of hurricane-like vorticity rings, *J. Atmos. Sci.*, *66*(3), 705–722.

Hopf, E. (1950), The partial differential equation $u_t+uu_x=\mu uu_x$, *Commun. Pure Appl. Math.*, *3*, 201–230.

Houze, R. A., S. Chen, B. F. Smull, W.-C. Lee, and M. M. Bell (2007), Hurricane intensity and eyewall replacement, *Science*, *315*, 1235–1239.

Huang, Y. H., M. T. Montgomery, and C. C. Wu (2012), Concentric eyewall formation in Typhoon Sinlaku (2008). Part II: Axisymmetric dynamical processes, *J. Atmos. Sci.*, *69*(2), 662–674.

Judt, F., and S. S. Chen (2010), Convectively generated potential vorticity in rainbands and formation of the secondary eyewall in Hurricane Rita of 2005, *J. Atmos. Sci.*, *67*(11), 3581–3599.

Kepert, J. D. (2001), The dynamics of boundary layer jets within the tropical cyclone core. Part I: Linear theory, *J. Atmos. Sci.*, *58*(17), 2469–2484.

Kepert, J. D. (2010a), Slab- and height-resolving models of the tropical cyclone boundary layer. Part I: Comparing the simulations, *Q. J. R. Meteorol. Soc.*, *136*, 1686–1699.

Kepert, J. D. (2010b), Slab- and height-resolving models of the tropical cyclone boundary layer. Part II: Why the simulations differ, *Q. J. R. Meteorol. Soc.*, *136*, 1700–1711.

Kepert, J. D., and Y. Wang (2001), The dynamics of boundary layer jets within the tropical cyclone core. Part II: Nonlinear enhancement, *J. Atmos. Sci.*, *58*(17), 2485–2501.

Large, W. G., J. C. McWilliams, and S. C. Doney (1994), Oceanic vertical mixing: A review and a model with a nonlocal boundary layer parameterization, *Rev. Geophys.*, *32*(4), 363–403.

Lee, C.-Y., and S. S. Chen (2012), Symmetric and asymmetric structures of hurricane boundary layer in coupled atmosphere-wave-ocean models and observations, *J. Atmos. Sci.*, *69*, 3576–3594.

Leveque, R. J. (2002), Finite Volume Methods for Hyperbolic Problems, Cambridge Texts in Applied Mathematics, Cambridge University Press, Cambridge, 558 pp.

Marks, F. D., P. G. Black, M. T. Montgomery, and R. W. Burpee (2008), Structure of the eye and eyewall of Hurricane Hugo (1989), *Mon. Weather Rev.*, *136*(4), 1237–1259.

Martinez, Y., G. Brunet, M. K. Yau, and X. Wang (2011), On the dynamics of concentric eyewall genesis: Space-time empirical normal modes diagnosis, *J. Atmos. Sci.*, *68*, 457–476.

Menelaou, K., M. K. Yau, and Y. Martinez (2012), On the dynamics of the secondary eyewall genesis in Hurricane Wilma (2005), *Geophys. Res. Lett.*, *39*, L04801, doi:10.1029/2011GL050699.

Montgomery, M. T., H. D. Snell, and Z. Yang (2001), Axisymmetric spindown dynamics of hurricane-like vortices, *J. Atmos. Sci.*, *58*(5), 421–435.

Moon, I.-J., I. Ginis, and T. Hara (2004), Effect of surface waves on Charnock coefficient under tropical cyclones, *Geophys. Res. Lett.*, *31*, L20302, doi:10.1029/2004GL020988.

Mrowiec, A. A., S. T. Garner, and O. M. Pauluis (2011), Axisymmetric hurricane in a dry atmosphere: Theoretical framework and numerical experiments, *J. Atmos. Sci.*, *68*, 1607–1619.

Musgrave, K. D., R. K. Taft, J. L. Vigh, B. D. McNoldy, and W. H. Schubert (2012), Time evolution of the intensity and size of tropical cyclones, *J. Adv. Model. Earth Syst.*, *4*, M08001, doi:10.1029/2011MS000104.

Nasuno, T., and M. Yamasaki (1997), The effect of surface friction on the mesoscale organization of cumulus convection in tropical cyclones, *J. Meteorol. Soc. Jpn.*, *75*(4), 907–924.

Ooyama, K. (1969a), Numerical simulation of the life cycle of tropical cyclones, *J. Atmos. Sci.*, *26*(1), 3–40.

Ooyama, K. (1969b), Numerical simulation of tropical cyclones with an axi-symmetric model, paper presented at the WMO/IUGG Symposium on Numerical Weather Prediction in Tokyo, 26 Nov.−4 Dec., 1968, Jpn. Meteorol. Agency, Tokyo.

Powell, M. D. (1990a), Boundary layer structure and dynamics in outer hurricane rainbands. Part I: Mesoscale rainfall and kinematic structure, *Mon. Weather Rev.*, *118*(4), 891–917.

Powell, M. D. (1990b), Boundary layer structure and dynamics in outer hurricane rainbands. Part II: Downdraft modification and mixed layer recovery, *Mon. Weather Rev.*, *118*(4), 918–938.

Powell, M. D., P. J. Vickery, and T. A. Reinhold (2003), Reduced drag coefficient for high wind speeds in tropical cyclones, *Nature*, *422*, 279–283.

Reul, N., H. Branger, and J.-P. Giovanangeli (1999), Air flow separation over unsteady breaking waves, *Phys. Fluids*, *11*, 1959–1961.

Rozoff, C. M., D. S. Nolan, J. P. Kossin, F. Zhang, and J. Fang (2012), The roles of an expanding wind field and inertial stability in tropical cyclone secondary eyewall formation, *J. Atmos. Sci.*, *69*(9), 2621–2643.

Schubert, W. H., M. T. Montgomery, R. K. Taft, T. A. Guinn, S. R. Fulton, J. P. Kossin, and J. P. Edwards (1999), Polygonal eyewalls, asymmetric eye contraction, and potential vorticity mixing in hurricanes, *J. Atmos. Sci.*, *56*(9), 1197–1223.

Shapiro, L. J. (1983), The asymmetric boundary layer flow under a translating hurricane, *J. Atmos. Sci.*, *40*(8), 1984–1998.

Sitkowski, M., J. P. Kossin, C. M. Rozoff, and J. Knaff (2012), Hurricane eyewall replacement cycle thermodynamics and the relict inner eyewall circulation, *Mon. Weather Rev.*, *140*, 4035–4045.

Smith, R. K. (2003), A simple model of the hurricane boundary layer, *Q. J. R. Meteorol. Soc.*, *129*, 1007–1027.

Smith, R. K., and M. T. Montgomery (2008), Balanced boundary layers used in hurricane models, *Q. J. R. Meteorol. Soc.*, *134*, 1385–1395.

Smith, R. K., and M. T. Montgomery (2010), Hurricane boundary-layer theory, *Q. J. R. Meteorol. Soc.*, *136*, 1665–1670.

Smith, R. K., and G. L. Thomsen (2010), Dependence of tropical-cyclone intensification on the boundary-layer representation in a numerical model, *Q. J. R. Meteorol. Soc.*, *136*, 1671–1685.

Smith, R. K., and S. Vogl (2008), A simple model of the hurricane boundary layer revisited, *Q. J. R. Meteorol. Soc.*, *134*, 337–351.

Smith, R. K., M. T. Montgomery, and S. Vogl (2008), A critique of Emanuel's hurricane model and potential intensity theory, *Q. J. R. Meteorol. Soc.*, *134*, 551–561.

Smith, R. K., M. T. Montgomery, and S. V. Nguyen (2009), Tropical cyclone spin-up revisited, *Q. J. R. Meteorol. Soc.*, *135*, 1321–1335.

Terwey, W. D., and M. T. Montgomery (2008), Secondary eyewall formation in two idealized, full-physics modeled hurricanes, *J. Geophys. Res.*, *113*, D12112, doi:10.1029/2007JD008897.

Wang, Y. (2008), Rapid filamentation zone in a numerically simulated tropical cyclone, *J. Atmos. Sci.*, *65*, 1158–1181.

Wang, Y. (2009), How do outer spiral rainbands affect tropical cyclone structure and intensity?, *J. Atmos. Sci.*, *66*, 1250–1273.

Whitham, G. B. (1974), *Linear and Nonlinear Waves*, 636 pp., John Wiley, New York.

Williams, G. J. (2012), The effects of environmental flow on the internal asymmetric dynamics of tropical cyclones, Ph.D. dissertation, 184 pp., Dep. of Atmos. Sci., Colorado State Univ., Fort Collins, Colo.

Willoughby, H. E., H.-L. Jin, S. J. Lord, and J. M. Piotrowicz (1984), Hurricane structure and evolution as simulated by an axisymmetric nonhydrostatic numerical model, *J. Atmos. Sci.*, *41*(7), 1169–1186.

Wu, C.-C., Y.-H. Huang, and G.-Y. Lien (2012), Concentric eyewall formation in Typhoon Sinlaku (2008). Part I: Assimilation of T-PARC data based on the ensemble Kalman filter (EnKF), *Mon. Weather Rev.*, *140*, 506–527.

Yamasaki, M. (1977), The role of surface friction in tropical cyclones, *J. Meteorol. Soc. Jpn.*, *55*(6), 559–572.

Yamasaki, M. (1983), A further study of the tropical cyclone without parameterizing the effects of cumulus convection, *Pap. Meteorol. Geophys.*, *34*, 221–260.

Zhang, J. A., and M. T. Montgomery (2012), Observational estimates of the horizontal eddy diffusivity and mixing length in the low-level region of intense hurricanes, *J. Atmos. Sci.*, *69*(4), 1306–1316.

Zhang, J. A., F. D. Marks, M. T. Montgomery, and S. Lorsolo (2011), An estimation of turbulent characteristics in the low-level region of intense Hurricanes Allen (1980) and Hugo (1989), *Mon. Weather Rev.*, *139*(5), 1447–1462.

Zhou, X., and B. Wang (2009), From concentric eyewall to annular hurricane: A numerical study with the cloud-resolved WRF model, *Geophys. Res. Lett.*, *36*, L03802, doi:10.1029/2008GL036854.

Zhou, X., and B. Wang (2011), Mechanism of concentric eyewall replacement cycles and associated intensity change, *J. Atmos. Sci.*, *68*(5), 972–988.

Corresponding author: R. K. Taft, Department of Atmospheric Science, Colorado State University, Fort Collins, CO 80523, USA. (taft@atmos.colostate.edu)